



HAL
open science

Imaging strain localisation in porous andesite using digital volume correlation

Michael J. Heap, Patrick Baud, Jessica A. Mcbeck, Francois Renard, Lucille Carbillet, Stephan A. Hall

► **To cite this version:**

Michael J. Heap, Patrick Baud, Jessica A. Mcbeck, Francois Renard, Lucille Carbillet, et al.. Imaging strain localisation in porous andesite using digital volume correlation. *Journal of Volcanology and Geothermal Research*, 2020, 404, pp.107038. 10.1016/j.jvolgeores.2020.107038 . insu-03094752

HAL Id: insu-03094752

<https://insu.hal.science/insu-03094752>

Submitted on 4 Jan 2021

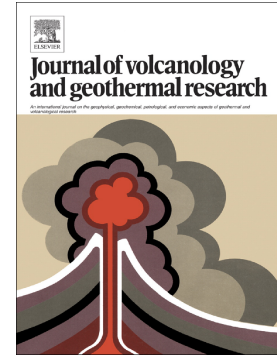
HAL is a multi-disciplinary open access archive for the deposit and dissemination of scientific research documents, whether they are published or not. The documents may come from teaching and research institutions in France or abroad, or from public or private research centers.

L'archive ouverte pluridisciplinaire **HAL**, est destinée au dépôt et à la diffusion de documents scientifiques de niveau recherche, publiés ou non, émanant des établissements d'enseignement et de recherche français ou étrangers, des laboratoires publics ou privés.

Journal Pre-proof

Imaging strain localisation in porous andesite using digital volume correlation

Michael J. Heap, Patrick Baud, Jessica A. McBeck, François Renard, Lucille Carbillet, Stephan A. Hall



PII: S0377-0273(20)30330-9

DOI: <https://doi.org/10.1016/j.jvolgeores.2020.107038>

Reference: VOLGEO 107038

To appear in: *Journal of Volcanology and Geothermal Research*

Received date: 10 June 2020

Revised date: 19 August 2020

Accepted date: 21 August 2020

Please cite this article as: M.J. Heap, P. Baud, J.A. McBeck, et al., Imaging strain localisation in porous andesite using digital volume correlation, *Journal of Volcanology and Geothermal Research* (2020), <https://doi.org/10.1016/j.jvolgeores.2020.107038>

This is a PDF file of an article that has undergone enhancements after acceptance, such as the addition of a cover page and metadata, and formatting for readability, but it is not yet the definitive version of record. This version will undergo additional copyediting, typesetting and review before it is published in its final form, but we are providing this version to give early visibility of the article. Please note that, during the production process, errors may be discovered which could affect the content, and all legal disclaimers that apply to the journal pertain.

© 2020 Published by Elsevier.

Imaging strain localisation in porous andesite using digital volume correlation

Michael J. Heap^{1*}, Patrick Baud¹, Jessica A. McBeck², François Renard^{2,3}, Lucille Carbillet¹, and Stephan A. Hall^{4,5}

¹*Géophysique Expérimentale, Institut de Physique de Globe de Strasbourg (UMR 7516 CNRS, Université de Strasbourg/EOST), 5 rue René Descartes, 67084 Strasbourg cedex, France*

²*Physics of Geological Processes, The Njord Centre, Department of Geosciences, University of Oslo, Norway*

³*Université Grenoble Alpes, Université Savoie Mont Blanc, CNRS, IRD, IFSTTAR, ISTERre, 38000 Grenoble, France*

⁴*Division of Solid Mechanics, Lund University, Lund 22100, Sweden*

⁵*Lund Institute for advanced Neutron and X-ray Science (LINXS), Scheelevägen 19, 22370 Lund, Sweden*

*Corresponding author. Michael Heap (heap@unistra.fr)

Highlights

- Shear fractures associated with localised dilation and permeability increase.
- Compaction bands associated with localised compaction and permeability decrease.
- Compaction bands form in the most porous part of the sample, within the well-connected porosity backbone.

- Geometric characteristics of compaction bands in lavas likely related to pore size and structure.
- Digital volume correlation is a useful tool to study strain localisation in porous volcanic rocks.

Abstract

Strain localisation structures, such as shear fractures and compaction bands, are of importance due to their influence on permeability and therefore outgassing, a factor thought to influence eruptive style. In this study, we aim to develop a better understanding of strain localisation in porous volcanic rocks using X-ray tomographic images of samples of porous andesite (porosity = 0.26) acquired before and after deformation in the brittle and ductile regimes. These 3D images have been first analysed to provide 3D images of the porosity structure within the undeformed andesite, which consists of a large, well-connected porosity backbone alongside many smaller pores that are either isolated or connected to the porosity backbone by thin microstructural elements (e.g., microcracks). Following deformation, porosity profiles of the samples show localised dilation (porosity increase) and compaction (porosity reduction) within the samples deformed in the brittle and ductile regimes, respectively. Digital volume correlation (DVC) of the images before and after triaxial deformation was used to quantify the tensor strain fields, and the incremental divergence (volumetric strain) and curl (used as an indicator of shear strain) of the displacement fields were calculated from the DVC. These fields show that strain localisation in the sample deformed in the brittle regime manifested as a ~1 mm-wide, dilatational shear fracture oriented at an angle of 40-45° to the maximum principal stress. Pre- and post-deformation permeability measurements show that permeability of the sample deformed in the brittle regime increased from 3.9×10^{-12} to $4.9 \times 10^{-12} \text{ m}^2$, which is presumed to be related to the

shear fracture. For the sample deformed in the ductile regime, strain localised into ~1 mm-thick, undulating compaction bands orientated sub-perpendicular to the maximum principal stress with little evidence of shear. Taken together, our data suggest that these bands formed during large stress drops seen in the mechanical data, within high-porosity zones within the sample, and within the large, well-connected porosity backbone. Pre- and post-deformation permeability measurements indicate that inelastic compaction decreased the permeability of the sample by a factor of ~3. The data of this study assist in the understanding of strain localisation in porous volcanic rocks, its influence on permeability (and therefore volcanic outgassing), and highlight an important role for DVC in studying strain localisation in volcanic materials.

Keywords: andesite; fracture; compaction band; permeability; X-ray computed tomography; digital image correlation

1 Introduction

Evidence for the localisation of strain in volcanoes and volcanic rocks is abundant. Lava domes contain abundant fractures (e.g., Anderson and Fink, 1990; Watts et al., 2002; Hale and Wadge, 2008; Buil et al., 2013; Darmawan et al., 2018). An impressive example of a lava dome fracture is the 200 m-long and 40 m-wide fracture that formed within the dome at Merapi volcano (Indonesia) following an explosion in 2013 (Walter et al., 2015). Lava spines are extruded along gouge rich conduit-margin faults (e.g., Iverson et al., 2006; Cashman et al., 2008; Kennedy and Russell, 2012; Hornby et al., 2015; Lamb et al., 2015; Ryan et al., 2018, 2020). The spines extruded at Mt St Helens (USA) from 2004 to 2008, for example, were mantled by a 1-3 m-thick layer of cataclasites, breccias, and gouge (e.g., Cashman et al., 2008). Ash-filled fractures within conduits and lava domes—called

tuffisites—record episodes of brittle deformation, magma fragmentation, and outgassing (e.g., Tuffen et al., 2003; Castro et al., 2014; Saubin et al., 2016; Farquharson et al., 2016a; Gardner et al., 2018; Heap et al., 2019a). Faults are also commonly observed in sequences of volcanic rock (e.g., Gudmundsson, 2011; Holland et al., 2006; Walker et al., 2013; Bubeck et al., 2018) and localised compaction features have been observed in outcrops of tuff (e.g., Wilson et al., 2003; Okubo, 2014; Cavailhes and Rotevatn, 2018). Furthermore, volcanic rocks can contain flow bands, defined by differences in the abundance and/or preferred orientation of crystals and/or pores (e.g., Tuffen et al., 2003; Pust et al., 2003; Castro et al., 2005; Gonnermann and Manga, 2005), that form as magmas deform on their way to the surface.

Strain localisation also plays an important role in governing the behaviour of volcanoes. For example, the permeability of a volcanic edifice is thought to exert control over whether a volcano erupts effusively or explosively (e.g., Eichelberger et al., 1986; Mueller et al., 2008; Cassidy et al., 2018) and fractures can serve to increase the permeability of volcanic rock (e.g., Nara et al., 2011; Walker et al., 2013; Farquharson et al., 2016b; Heap and Kennedy, 2016). Strain localisation can also negatively influence the stability of volcanic structures (e.g., Voight, 2000; Lagmay et al., 2000), the collapse of which can result in the formation of destructive and deadly pyroclastic density currents (e.g., Glicken, 1996; Cole et al., 1998; Komorowski et al., 2013).

The failure mode of volcanic rock (i.e. volcanic materials below their glass transition threshold) depends, to a first order, on the confining pressure (i.e. depth) and the porosity of the rock: low pressure and low porosity favour brittle deformation and high pressure and high porosity favour shear-enhanced compaction (e.g., Zhu et al., 2011; Heap et al., 2015a). Although temperature can affect the mechanical behaviour of volcanic materials below their glass transition threshold, fully- or almost-fully-crystallised lavas were still brittle at high

temperature (700-950 °C; Benson et al., 2012; Heap et al., 2018). In volcanic rocks, strain localises into shear and tensile fractures in the brittle regime (e.g., Benson et al., 2007; Heap and Kennedy, 2016; Zhu et al., 2016). At relatively high effective pressures, laboratory studies have shown that inelastic compaction in volcanic rocks can either be distributed, termed “cataclastic flow” (e.g., Zhu et al., 2011), or localised into bands (e.g., Loaiza et al., 2012; Adelinet et al., 2013; Heap et al., 2015a). Both cataclastic flow and the formation of compaction bands, planar deformation features characterised by a lower porosity than the surrounding host rock, are often considered as ductile behaviour. Laboratory experiments have shown that shear (Fortin et al., 2011; Walker et al., 2015; Farquharson et al., 2016b) and tensile fractures (e.g., Nara et al., 2011; Heap and Kennedy, 2016; Eggertsson et al., 2020) involve dilatancy and can increase the permeability of volcanic rock by many orders of magnitude. Rare studies on the influence of compaction bands on the permeability of volcanic rock have shown that they can decrease sample permeability by up to about one order of magnitude (Heap et al., 2015a; Farquharson et al., 2017).

Microstructural analysis on laboratory-deformed samples have highlighted that the dilatant fracture of volcanic rocks involves a complex interplay between microcracks, pores, and phenocrysts (e.g., Zhu et al., 2016). Fractures are seen to emanate from pores and propagate through both groundmass and phenocrysts (e.g., Zhu et al., 2011; Heap et al., 2014; Heap et al., 2015a; Zhu et al., 2016; Coats et al., 2018). Tensile fractures in andesite were found to be more tortuous as a function of increasing porosity (Heap and Kennedy, 2016). Benson et al. (2007) imaged the growth of a shear fracture in a low-porosity basalt from Mt Etna (Italy) by locating acoustic emissions (i.e. microcrack formation and growth; Lockner, 1993) within the sample during deformation. These authors found that the fracture, which formed an inclined plane within the sample, propagated from the lower right-hand to the upper left-hand part of the sample. The shear fracture grew at a speed of $\sim 4 \text{ mm.s}^{-1}$ at its

leading edge and $\sim 2 \text{ mm.s}^{-1}$ at its centre; this is considerably slower than the shear fracture growth speed for granite (Benson et al., 2007). McBeck et al. (2019) studied shear fracture formation in the same low-porosity basalt using digital volume correlation (DVC) techniques and found that the strain localisation process started before the peak stress and was preceded by phase of compaction. However, studies aimed at studying strain localisation in the brittle regime in porous volcanic rocks using techniques other than microscopy are currently absent.

Compared to our understanding of compaction band formation in porous sedimentary rocks, our understanding of this process in volcanic rocks is embryonic. Compaction bands were first documented in sandstone (Hill, 1989; Mollema and Antonellini, 1996) and later in carbonate (Cilona et al., 2014; Rotevatn et al., 2016) formations. Field, laboratory, and numerical studies have shown that subtle differences in microstructural attributes, such as grain size distribution, can promote or inhibit the development of compaction bands in granular materials (Wang et al., 2008; Chung et al., 2012). Compaction bands formed in laboratory deformation experiments typically have a thickness of 2-4 grains, are oriented sub-perpendicular to the maximum principal stress, initiate at one side of the sample and propagate to the other, are associated with intense grain crushing and pore collapse, and their growth is marked by an uptick in acoustic emission activity (e.g., Baud et al., 2004; Louis et al., 2006; Fortin et al., 2006; Townend et al., 2008; Charalampidou et al., 2011; Heap et al., 2015b; Baud et al., 2015; Huang et al., 2019; Shahin et al., 2019). Compaction bands have also been found in porous tuffs (Cavailhes and Rotevatn, 2018) and laboratory studies on volcanic rocks have, so far, observed compaction bands in porous basalt (Adelinet et al., 2013), porous trachyandesite (Loaiza et al., 2012), porous andesite (Heap et al., 2015a, 2017), and porous dacite (Heap et al., 2016). The compaction bands observed in these laboratory studies on volcanic rocks have shown some geometric similarities with those observed in sedimentary rocks. However, because the studied rocks were all lavas (i.e. non-granular), the

compaction bands formed in these samples were planes of collapsed pores connected by microcracks that formed sub-perpendicular to the maximum principal stress. It is likely therefore that the geometry of compaction bands in volcanic rock depends on the distribution of pores within the sample (as discussed in Heap et al., 2015a).

In this study, we selected a porous andesite from Volcán de Colima (Mexico) for which extensive sets of petrophysical and mechanical data were recently published (e.g., Heap et al., 2017). We first used X-ray Computed Tomography (CT) to detail the complexity of the void space within the andesite. CT has been used to study the topology of the pore space of simple rocks such as Fontainebleau sandstone (Lindquist et al., 2000) and more microstructurally complex porous rocks (e.g., Bauer et al., 2012; Fousseis et al., 2012; Ji et al., 2012; Kandula et al., 2019). The microstructure of lavas (e.g., Song et al., 2001; Jamtveit et al., 2011, 2014; Pola et al., 2012; Bubeck et al., 2017; Schipper et al., 2017) and high-porosity (> 0.5) scoria and pumice (e.g., Polacci et al., 2006; Zandomenighi et al., 2010; Degruyter et al., 2010; Baker et al., 2011; Voltolini et al., 2011; Giachetti et al., 2011; Pardo et al., 2014) have been studied using CT. CT has also been used to study porosity loss by viscous sintering in granular materials in volcanic systems (Wadsworth et al., 2017, 2019) and particle size and shape in tuffisites (Black et al., 2016).

In this work, our main objective is to use 3D CT image data to better understand the development of strain localisation in andesite deformed in the brittle and ductile regimes. Brittle and ductile are used herein to describe the deformation on the lengthscale of a laboratory sample. Brittle deformation is synonymous with the formation of a macroscopic shear fracture and, although ductile deformation typically “describes the capacity of a material to deform to substantial strain without the tendency to localise the flow into bands (faults)” (Rutter, 1986), this simple definition is complicated by instances of compaction localisation in the ductile regime (Wong and Baud, 2012). Here, samples that contain

compaction localisation are considered ductile. Our concept of ductility does not depend on the micromechanisms of deformation and, therefore, ductility in volcanic materials is not restricted to viscous flow.

Previous studies showed that CT imaging, even with limited resolution, could reveal shear bands in laboratory deformed sandstone (see, for example, Bésuelle et al., 2003). However, imaging failure in complex rocks such as shales or compaction localisation in sandstone typically requires image analysis (e.g., Louis et al. 2006; Lenoir et al., 2007). For example, digital image correlation techniques were used to investigate strain localisation in sedimentary rocks (e.g., Louis et al., 2007; Charalampidou et al., 2010; Dautriat et al., 2011; Ji et al., 2015; Tudisco et al., 2015; McBeck et al., 2018; Penard et al., 2017, 2019; McBeck et al., 2020). Recently, digital volume correlation (DVC) was used to study failure in low-porosity basalt from Mt Etna using in situ X-ray synchrotron microtomography (McBeck et al., 2019). However, such high-resolution imaging ($6.5 \mu\text{m}/\text{voxel}$) can only be performed on very small samples (the sample deformed in the study of McBeck et al. (2019) was a 3.7 mm-diameter cylinder) and therefore is ill-suited to capture porosity development in the vast majority of porous volcanic rocks, which often contain pores above 1 mm in diameter (e.g., Shea et al., 2010; Heap et al., 2014). Here, we perform DVC on X-ray images of porous andesite deformed in both the brittle and ductile regimes to study the development of shear fractures and compaction bands in porous volcanic rock. To avoid issues with large pores, we used a standard laboratory sample size (20 mm-diameter cylinders) and therefore a lower imaging resolution ($23 \mu\text{m}/\text{voxel}$) than McBeck et al. (2019).

2 Material characterisation and methods

The block of andesite used for this study was collected from within a debris-flow track (“La Lumbre”) on the flanks of Volcán de Colima (Mexico; Figure 1a). Volcán de

Colima is an active andesitic stratovolcano located in the Trans-Mexican Volcanic Belt (Varley et al., 2019; Figure 1a). This block of andesite is the same as that used for the study of Heap et al. (2017), and similar to those used in recent uniaxial and triaxial deformation studies (Lavallée et al., 2013; Kendrick et al., 2013; Heap et al., 2014, 2015a). Heap et al. (2017) showed the brittle-ductile transition for the studied andesite occurs at an effective pressure (confining pressure minus the pore fluid pressure) between 20 and 30 MPa and that it forms compaction bands when deformed at high pressure, and so it is an ideal material for this study. The andesite has a porphyritic texture that contains phenocrysts of plagioclase and pyroxene and irregularly-shaped pores (with radii from a couple of tens of microns to ~ 500 μm) within a glassy groundmass (that contains abundant microlites, mainly plagioclase with subordinate high-density Fe-Ti oxides) (Figure 1b shows a backscattered scanning electron microscope (SEM) image). The volume fraction of phenocrysts is ~ 0.4 and the groundmass consists of microlite and glass volume fractions of ~ 0.2 and ~ 0.135 , respectively (Heap et al., 2017). The andesite also contains abundant microcracks (Figure 1b).

Two cylindrical samples, 20 mm in diameter and 40 mm in length, were prepared from the block and dried in a vacuum-oven at a temperature of 40 °C for at least 48 hours. The connected porosity of these samples was then calculated using the bulk sample volume and the skeletal volume measured by a helium pycnometer. Their total porosity was calculated using the skeletal density of the block (calculated using the mass and volume, measured using the pycnometer, of a powdered aliquot of the block) and the bulk sample density. The permeability of the two samples was then measured under a confining pressure of 1 MPa using a benchtop gas (nitrogen) permeameter (see Heap and Kennedy, 2016). The samples were first left at 1 MPa for 1 hour to ensure microstructural equilibrium. Volumetric flow rates (measured using a gas flowmeter) were then measured for six pore pressure

differentials (measured using a pore pressure transducer) to calculate permeability using Darcy's law and to check if Forchheimer or Klinkenberg corrections were required.

X-ray tomography images were made of the samples at the 4D Imaging Laboratory at Lund University (Sweden) using a ZEISS Xradia 520 Versa 3D X-ray microscope. Tomography, with cubic voxels of side length 23 μm , were acquired before and after triaxial deformation. Figure 2 presents a 2D vertical slice extracted from the 3D image volume of sample LL3, which shows the features (pores and phenocrysts) observed in the SEM image (Figure 1b). Figure 2 also shows a histogram of the X-ray attenuation coefficient for the CT image volume as a function of grey level, where 0 (lowest attenuation) and 255 (highest attenuation) correspond to black and white, respectively. The two peaks at a grey level of ~ 13 and ~ 63 correspond to the porosity (macropores) and the glassy groundmass, respectively (Figure 2). Values of grey level above that of the groundmass ($> \sim 80$) correspond to the denser plagioclase phenocrysts and values of grey level between the two main peaks correspond to pixels that contain both groundmass and porosity (microporosity) (Figure 2). If we segment the images (porosity was taken as all the voxels with a grey level lower than the minimum following the first peak in X-ray attenuation (corresponding to the macropores) within the sample, as indicated in Figure 2), a 3D image of the porosity structure can also be generated (Figure 3). The 3D images in Figure 3 were prepared using Avizo® Fire 3D visualisation and analysis software. Figure 3a shows a 3D image that highlights all of the porosity (each connected pore is shown in a different colour) within one of the samples (sample LL3). The large, dark blue-coloured pore represents the well-connected porosity backbone of the sample (Figure 3a). The pores unconnected to this backbone, or connected to the porosity backbone by very thin microstructural elements (e.g., microcracks) that have a size below the scanning resolution, are best observed when this large, well-connected connected pore is removed from the image (Figure 3b). The porosity structure of the porous

andesite studied can, therefore, be considered to consist of a large, well-connected porosity backbone alongside many smaller pores that are either isolated or connected to the porosity backbone by very thin microstructural elements (e.g., microcracks) (Figure 3). Figure 3c shows the equivalent pore radius distribution for these isolated or poorly-connected pores. We measure no pores with a radius below $75\ \mu\text{m}$, which is likely a function of the voxel size ($23\ \mu\text{m}/\text{voxel}$). Indeed, pores with a radius $< 75\ \mu\text{m}$ are seen in the SEM image of the studied material (Figure 1b). The majority of the isolated or poorly-connected pores detected in the X-ray images have a radius between 100 and $200\ \mu\text{m}$ (Figure 3c), and the average pore radius is $126\ \mu\text{m}$.

Prior to deformation in the triaxial press, performed at the University of Strasbourg (France), both samples were vacuum-saturated in deionised water and wrapped in a thin ($\ll 1\ \text{mm}$) copper jacket. The thin copper jacket helps to protect the integrity of the sample during unloading, but does not influence the mechanical behaviour of the sample during deformation. The samples were inserted into a Viton[®] rubber sleeve and placed inside the pressure vessel. The confining and pore fluid pressure were then slowly increased using servo-controlled confining and pore fluid pressure pumps, respectively, to the chosen pressure (either 20 or $60\ \text{MPa}$ for the confining pressure and $10\ \text{MPa}$ for the pore fluid pressure). We assume here a simple effective pressure law where the effective pressure is equal to the confining pressure minus the pore fluid pressure. The samples were then left overnight at the target effective pressure to ensure microstructural equilibration. The samples were subsequently deformed in compression at an axial strain rate of $10^{-5}\ \text{s}^{-1}$. During deformation we recorded axial load and displacement, which were converted to axial stress and strain using the sample dimensions, and the change in sample porosity (monitored by the pore fluid pump). We note that measured values of axial stress and strain and porosity correspond to bulk sample measurements. During deformation, the confining and pore fluids

pressures were held constant by the servo-controlled pumps. Sample drainage during deformation was ensured by the high permeability of the studied material ($> 10^{-12} \text{ m}^2$; Heap and Wadsworth, 2016). The sample deformed at an effective pressure of 10 MPa was unloaded at a strain rate of 10^{-5} s^{-1} immediately following the large stress drop typically associated with the formation of a macroscopic shear fracture. The sample deformed at an effective pressure of 50 MPa was unloaded following deformation to an axial strain of 0.015. These samples were then dried completely in a vacuum-oven and re-scanned, as described above. The sample deformed at an effective pressure of 50 MPa was then re-saturated, deformed again at the same conditions to an axial strain of 0.015, carefully unloaded, dried, and then scanned a third time. Finally, the permeability of the deformed samples was re-measured using the above-described method. Both our triaxial deformation experiments and permeability measurements were performed under ambient laboratory temperatures.

The magnitude and spatial distribution of the volumetric and distortional strain components were calculated using the TomoWarp2 DVC code (Tudisco et al., 2017) using the tomography images acquired before and after deformation. Using these displacement fields, we calculated divergence and curl fields using by matching voxel constellations between the sequential X-ray image acquisitions. Negative and positive divergence corresponds to compaction and dilation, respectively, and negative and positive curl corresponds to left-lateral and right-lateral rotations, respectively, indicative of shear strain. We used Moran's I coefficient (Moran, 1948) to determine the spatial localisation of the incremental strain populations (e.g., Zhang and Lin, 2016; Thompson et al., 2018; McBeck et al., 2019). We refer the reader to Tudisco et al. (2017) and McBeck et al. (2019) for more information on the DVC technique used here.

3 Results

3.1 Porosity and permeability data

The connected porosities, measured by the pycnometer, of samples LL5 and LL3 were 0.256 and 0.262, respectively. The skeletal density of the block was measured to be 2669 kg/m³, which yields total porosities for LL5 and LL3 of 0.261 and 0.269, respectively, and isolated porosities of 0.006 and 0.005, respectively. The intact permeabilities of samples LL5 and LL3 were 3.9×10^{-12} and 4.7×10^{-12} m², respectively. Following deformation, the permeabilities of samples LL5 and LL3 were 4.9×10^{-12} and 1.5×10^{-12} m², respectively.

3.2 Mechanical data

The stress-strain curves and porosity reduction curves for both samples (LL5 and LL3) are shown in Figure 4. The mechanical data for the sample deformed at an effective pressure of 10 MPa (LL5) are typical for a rock sample deforming in compression in the brittle regime (e.g., Brace et al., 1966; Scholz, 1968). Differential stress is first a non-linearly increasing function of axial strain, often attributed to the closure of pre-existing microcracks, followed by a quasi-linear elastic stage. Differential stress is then non-linearly increasing function of axial strain, attributed to the formation and growth of microcracks (i.e. inelastic deformation). A peak stress can be observed in the stress-strain data at ~93 MPa, which is followed by a stress drop (Figure 4a). It is during this stress drop that microcracks coalesce to form a macroscopic fracture. The porosity data show that the rock first compacted, the rate of which slowed above the stress required for the formation and propagation of microcracks, termed C' (at ~30 MPa; Figure 4c). Compaction and dilation were balanced at a differential stress of ~70-80 MPa (corresponding to an axial strain of ~0.005 and a porosity decrease of ~0.0025). Above this stress, the rock entered a phase of net dilation (Figure 4c). Porosity was increased by 0.001 during this phase and, at the end of the loading part of the experiment, the

porosity of the sample had been reduced by 0.0015 (Figure 4c). The porosity of the sample decreased during the unloading part of the experiment and the final porosity change of the sample (i.e. at the point of the second scan) was a reduction of 0.0021 (Figure 4c).

The mechanical data for the sample deformed at an effective pressure of 50 MPa are typical for porous andesite deforming in compression in the ductile regime (e.g., Heap et al., 2015a; Heap et al., 2017). Indeed, previous experimental studies that the stress-strain curves of lava deforming in the ductile regime can be punctuated by stress drops, considered to be associated with the formation of compaction bands (e.g., Heap et al., 2015a, 2017). A large stress drop (> 70 MPa) can be seen in the stress-strain data for the first loading-unloading experiment, after which the stress increases (Figure 4b). The porosity data show that the rock compacted throughout the experiment (Figure 4d). At the end of the first loading-unloading experiment (i.e. at the point of the second scan), the porosity of the sample had been reduced by 0.01 (Figure 4d). During the second loading-unloading experiment, we note another large stress drop during the loading stage, of about 40 MPa (Figure 4b). At the end of the second loading-unloading experiment (i.e. at the point of the third scan), the sample had lost a porosity of 0.019 (Figure 4d).

3.3 Porosity profiles before and after deformation

Figure 5 shows porosity profiles along the length of the samples deformed in the brittle (LL5) and ductile (LL3) regimes before and after deformation. The porosity was taken as all the voxels with a grey level lower than the minimum following the first peak in X-ray attenuation (corresponding to the macropores) within the sample (indicated in Figure 2). Although this approach underestimates the porosity, as micropores smaller than the voxel size are not captured, it provides data for the intact and deformed samples that can be confidently compared. The sample edges were excluded from this analysis.

The porosity profiles of the sample deformed in the brittle regime show that, following deformation, the porosity of the sample notably increased (by almost 0.01) between a distance of ~25 to ~30 mm along the sample length (Figure 5a). The average porosity of the sample determined using this technique increased from 0.128 to 0.130 following deformation. The porosity profiles for the sample deformed in the ductile regime show that, following the first round of deformation (see Figure 4c), the porosity of the sample was largely unchanged (Figure 5b). The average porosity of the sample increased slightly following the first round of deformation, from 0.150 to 0.153. By contrast, the mechanical data indicate that the sample was compacting during this stage (Figure 4d). Following the second round of deformation, the porosity between a distance of ~25 to ~33 mm along the sample length decreased by up to 0.04, and the average porosity of the sample decreased from 0.153 to 0.147 (Figure 5b). As discussed above, this method underestimates the porosity because it does not capture the microporosity. For example, the connected porosity of LL5 and LL3 prior to deformation was measured using the pycnometer to be 0.256 and 0.262, respectively.

3.4 Digital volume correlation (DVC)

The strain fields derived from the DVC are presented in Figure 6, as vertical slices through the 3D volume of divergence (volumetric strain) and curl magnitude (a proxy for shear strain). The DVC for the sample deformed in the brittle regime (LL5) shows clear evidence of strain localisation (Figure 6a). The feature, orientated at an angle of 40-45° to the maximum principal stress with a width of ~1 mm, is a planar volume characterised by elevated dilation and shear (Figure 6a). The remainder of the sample (i.e. outside the localisation feature) is characterised by dilation and low shear (apart from the bottom left and top right of the sample) (Figure 6a). The first loading-unloading experiment in the ductile regime does not show any clear localisation features (Figure 6b). In contrast to the

mechanical data, which show that the sample experienced compaction (Figure 4d), the DVC maps show that the sample is characterised by distributed dilation and low shear strain (Figure 6b). The second loading-unloading experiment in the ductile regime shows clear evidence for strain localisation (Figure 6c). The feature, orientated sub-perpendicular to the maximum principal stress with a thickness of ~ 1 mm, is a planar volume characterised by compaction and very little shear (Figure 6c). The remainder of the sample (i.e. outside the localisation feature) is characterised by compaction (apart from the bottom left of the sample and adjacent to the compaction feature) and high shear (Figure 6c).

4 Discussion

Based on their geometrical attributes, we interpret the inclined dilatational plane and the sub-horizontal compaction plane in the brittle and ductile regimes as a dilatational shear band and a compaction band, respectively.

4.1 Shear fractures in porous volcanic rocks

The shear fracture within the porous andesite sample is oriented at an angle of $40\text{-}45^\circ$ to the maximum principal stress (Figure 6a), formed within a high-porosity zone of the sample (Figure 5a), has a width of ~ 1 mm (Figure 6a), and is characterised by an increase in porosity (Figure 5a and Figure 6a). Our permeability data show that the permeability of the sample was higher after deformation, which we attribute to the shear fracture.

Shear fracture formation in low-porosity rocks, such as granite, results in dilation and large increases to sample permeability (e.g., Mitchell and Faulkner, 2008). Shear bands in high-porosity sandstone, however, can either be dilatant or compactant (e.g., Bésuelle, 2001). Laboratory studies have shown that both dilatant and compactant shear bands reduce the permeability of porous sandstone (e.g., Zhu and Wong, 1997). Laboratory studies have also

shown that shear fractures in basalt and andesite can increase sample permeability by three orders of magnitude (Farquharson et al., 2016b); however, the experiments of Farquharson et al. (2016b) were restricted to samples with initial porosities < 0.15 . Experiments on sandstones show that decreases to sample permeability are seen following brittle failure when the initial porosity is > 0.15 , interpreted as a result of a dramatic increase in void space tortuosity due to microcracking (Zhu and Wong, 1997). However, it was unclear whether a porous volcanic rock (porosity > 0.15), with a microstructure characterised by an amorphous glassy groundmass that hosts pores (compared to the granular microstructure presented by sandstone), would also exhibit a decrease in sample permeability following brittle failure. Our new data show that a shear fracture that formed in an andesite with an initial porosity of ~ 0.26 at low effective pressure was associated with localised dilation (i.e. porosity increase) on the fracture (Figures 5a and 6a) and a net increase in porosity throughout the sample (Figure 6a). A small increase in sample permeability (from 3.9×10^{-12} to $4.9 \times 10^{-12} \text{ m}^2$) was also observed following the formation of a dilatant shear fracture. This relatively small increase is considered to be the consequence of the high initial permeability of the sample: fractures in laboratory samples exert a much greater influence on the permeability of low-porosity, low-permeability volcanic rocks (e.g., Heap and Kennedy, 2016). We note that compactional shear bands may form in the studied andesite at higher effective pressures, but below the pressure required for the brittle-ductile transition (between 20 and 30 MPa; Heap et al., 2017), which may result in reductions to sample permeability. Systematic laboratory experiments are now required to investigate the influence of shear bands (both dilational, as studied here, and compactional shear bands that form at higher effective pressures) on the permeability of porous volcanic rocks.

4.2 Compaction bands in porous volcanic rocks

Our porosity analysis data (Figure 5b) and DVC data (Figure 6b) show that there was a net increase in porosity following the first round of deformation in the ductile regime. These data are in conflict with our mechanical data, which show that the sample compacted during deformation (Figure 4d). The reason for this discrepancy is because the compaction band that formed following the first round of deformation was located at the top of the sample (Figure 7) and was therefore not included in the porosity (Figure 5b) or DVC analyses (Figure 6b). During the second round of deformation, however, we see clear evidence for a compaction band in both the porosity data (Figure 5b) and the DVC analyses (Figure 6c). There are, therefore, two compaction bands in the sample following the second loading-unloading experiment. The formation of these compaction bands likely occurred during the two large stress drops (associated with porosity reduction) seen in the mechanical data (Figures 4b and 4d), as previously observed during compaction band formation in sandstones (Baud et al., 2004). The stress drops seen in our mechanical data (Figure 4b) are therefore the result of the formation of bands of collapsed pores within the sample. This hypothesis is also supported by the fact that the compaction band formed during the first loading-unloading cycle did not increase in thickness following the second round of deformation.

The average thickness of the compaction band formed during the second round of deformation (imaged with the porosity and DVC analysis) is ~ 1 mm (Figure 6c) and, as a result of its undulating geometry (the tortuosity of the band in the slice shown in Figure 6c is 1.48), affects a zone that is ~ 8 mm wide (Figure 5b; Figure 6c). The porosity profile data show that this compaction band formed within the most porous part of the sample (Figure 5b). We further note that the number of isolated or poorly-connected pores in the sample following the second round of deformation, and their average radius and radius distribution, were very similar to the undeformed sample. For example, the average pore radius was 126

μm in both cases. These data suggest that the compaction band formed within the large, well-connected porosity backbone of the sample (shown in blue in Figure 3a).

A compaction band thickness of ~ 1 mm is larger than seen in porous sandstones, where compaction bands are typically only 500-600 μm in thickness (two to four grains-thick; e.g., Tembe et al., 2008; Baud et al., 2012). Compaction band thicknesses of 1-3 mm have been observed in previous experimental studies on porous basalt (Adelinet et al., 2013), porous trachyandesite (Loaiza et al., 2012), porous andesite (Heap et al., 2015a, 2017), and porous dacite (Heap et al., 2016). The magnitude of stress drops seen in the mechanical data (Figure 4b), which are much larger than those seen in experiments on sandstone, are likely the result of this difference in compaction band thickness. Because compaction bands in lavas form as a result of cataclastic pore collapse, it follows that the thickness of the compaction bands that form in these materials will be close to the pore diameter, the largest of which is > 1 mm in the studied lavas. We suggest that, because the compaction band in our andesite formed within the most porous part of the sample (Figure 5b), the zone that also likely contains the largest pores, the thickness of compaction bands in lava will likely approach the diameter of the largest pore. Experiments on volcanic rocks that contain greatly different pore sizes and different pore structures (e.g., connectivity) are now required to explore this hypothesis.

The formation of compaction bands in sandstones requires a relatively homogeneous grain size distribution (e.g., Wang et al., 2008; Cheung et al., 2012). Within this narrow grain size distribution, compaction bands in sandstones have been characterised as either discrete or diffuse, where discrete bands propagate from one side of the sample to the other and diffuse bands are the result of the development of several small discrete bands (e.g., Baud et al., 2004). Sandstones that form discrete compaction bands are typically more microstructurally homogenous than those that form diffuse compaction bands (e.g., Louis et

al., 2007). Our study, and previous studies (Loaiza et al., 2012; Adelinet et al., 2013; Heap et al., 2015a, 2016, 2017), has shown that, unlike sandstones, compaction bands can form in very microstructurally complex and heterogeneous lavas. Studies on compaction bands in volcanic rocks, including the present study, have also shown that these compaction bands do not appear to consist of several small discrete bands: they appear to propagate as a single entity from one side of the sample to the other, rather like a discrete compaction band (Figure 6c). However, although the compaction bands that form in lavas could be considered discrete, discrete compaction bands in sandstones are typically characterised by a low tortuosity (e.g., Vajdova et al., 2003; Baud et al., 2004; Stanchits et al., 2005). By contrast, the tortuosity of the compaction band imaged here (Figure 6c), and that of bands formed in previous studies (Loaiza et al., 2012; Adelinet et al., 2013; Heap et al., 2015a, 2016, 2017), is significantly higher. Because the compaction band imaged in this study formed in the zone of highest porosity (Figure 5b), the tortuosity of the band was therefore governed by the shape of porosity backbone from one side of the sample to the other within this zone (the band can only exist where there are pores). Since this porosity network is unlikely to be planar from one side of the sample to the other in such porous volcanic rocks (e.g., Figure 3a), compaction bands in porous volcanic rocks are very likely to present tortuous geometries, as observed here (Figure 6c) and in other studies (e.g., Heap et al., 2015a).

Compaction bands in sandstone can reduce sample permeability by 2-3 orders of magnitude (e.g., Vajdova et al., 2004; Baud et al., 2012). The strain required to achieve this reduction in permeability depends on how much strain is required to form an efficient barrier, and more strain is required in sandstones that develop diffuse compaction bands compared to those that develop discrete compaction bands (e.g., Vajdova et al., 2004; Baud et al., 2012). Although compaction bands in lavas could be considered discrete, it is clear from our permeability measurements that they do not form an efficient barrier to fluid flow.

Measurements showed that the permeability of sample LL3 was only reduced by a factor of ~ 3 following deformation to an axial strain of 0.03. Heap et al. (2015a) showed that permeability of another andesite from Volcán de Colima was reduced by a factor of ~ 3 at an axial strain of 0.015 and by about one order of magnitude at an axial strain of 0.045. Farquharson et al. (2017) also showed that axial strains > 0.015 are required for permeability reductions of an order of magnitude in porous andesite. It is clear that, unlike in sandstones, compaction bands in porous lavas do not form an efficient barrier to fluid flow, a difference likely related to the complex nature of the well-connected porosity structure in these porous rocks (e.g., Figure 3a). Systematic laboratory experiments are now required to further investigate compaction localisation in porous volcanic rocks and its influence on permeability.

4.3 Volcanological implications

A detailed understanding of strain localisation in volcanic rocks is required due to the influence of shear fractures and compaction bands on permeability—a metric considered to influence volcanic character (e.g., Eichelberger et al., 1986; Mueller et al., 2008; Cassidy et al., 2018; Heap et al., 2019b)—and on dome and flank stability, the collapse of which can generate pyroclastic density currents with potentially dire humanitarian and economic consequences (e.g., Cole et al., 1998; Komorowski et al., 2013). Our study shows that, unlike porous sandstones (e.g., Zhu and Wong, 1997), the permeability of high-porosity volcanic rocks increases following shear fracture formation at low effective pressure. An increase in the permeability of edifice-forming rocks could increase the efficiency of outgassing (e.g., Collinson and Neuberg, 2012), thus promoting effusive volcanic behaviour. Importantly, brittle deformation in porous lavas (at low effective pressure) may not be associated with decreases to permeability, as seen for sandstones of similar porosity (e.g., Zhu and Wong,

1997). In the ductile regime (i.e. at a depth between 1 and 1.5 km), compaction bands will form within high-porosity zones and result in the compaction of the well-connected, porosity backbone that supports high permeability. Therefore, although compaction bands in lavas form within a microstructurally complex and well-connected porosity backbone, a factor that may limit the extent to which they reduce permeability (compared to sandstones; Vajdova et al., 2004; Baud et al., 2012), they are associated with reductions to permeability (as seen in previous laboratory studies: Heap et al., 2015a; Farquharson et al., 2017). A decrease in the permeability of edifice-forming rocks could decrease the efficiency of outgassing (e.g., Collinson and Neuberg, 2012), thus promoting explosive volcanic behaviour. Finally, we note that compaction bands in volcanic edifices will also create a permeability anisotropy, an important consideration in volcanic systems (e.g., Farquharson and Wadsworth, 2018).

5 Conclusions

To better understand strain localisation in porous volcanic rocks, we performed porosity and DVC analyses on X-ray computed tomography images of porous andesite deformed in the brittle and ductile regimes. These analyses reveal that strain localisation in a sample deformed in the brittle regime manifested as a ~1 mm-wide, dilatational shear fracture orientated at an angle of 40-45° to the maximum principal stress. For a sample deformed in the ductile regime, strain localised into ~1 mm-thick, undulating compaction bands orientated sub-perpendicular to the maximum principal stress with little evidence of shear. These compaction bands likely formed following stress drops seen in the mechanical data and formed within the zones of highest porosity, within the large, well-connected porosity backbone of the sample. Shear fracturing in the brittle regime and the formation of compaction bands in the ductile regime were seen to result in an increase and decrease in sample permeability, respectively. Our study also highlights that X-ray tomography

combined with DVC can provide insight into deformation and strain localisation in porous volcanic rocks, the importance of which is emphasised by their influence on, for example, permeability and therefore outgassing and eruption style (effusive or explosive). DVC on a wide range of volcanic rocks (characterised by different pore sizes and shapes and pore structures), coupled with laboratory measurements of permeability, offers an exciting avenue for future research.

Acknowledgements

We thank Thierry Reuschlé and Erika Tudisco. Nick Varley and Jamie Farquharson are thanked for their help in collecting the andesite block. This study was funded by LabEx Grant ANR-11-LABX-0050_G-EAU-THERMIE-FRUFONDE (this research therefore benefited from state funding managed by the Agence National de la Recherche (ANR) as part of the “Investissements d’avenir” program). Funding for this project was also provided by the Research Council of Norway: grant 272217 (ARGUS) to François Renard and grant 300435 to Jess McBeck. Lucille Carbillet acknowledges funding from the Doctoral School at the University of Strasbourg. X-ray images can be made available on request. The comments of two anonymous reviewers helped improve this manuscript.

Figure captions

Figure 1. (a) Image from GoogleEarth© showing Volcán de Colima (height = 3820 m), Mexico. The block of andesite used for this study was collected in the “La Lumbre” debris flow track and is indicated by the white arrow. Inset shows a map of Mexico showing the location of Volcán de Colima (the red triangle). (b) Backscattered scanning electron microscope image of the studied andesite. The porosity is shown in black.

Figure 2. Histogram of the grey-scale values of the X-ray tomography data for sample LL3. The grey-scale indicates the relative X-ray attenuation coefficient, where 0 is black (lowest attenuation) and 255 is white (highest attenuation). Inset: 2D vertical slice extracted from the 3D X-ray tomography image of the undeformed LL3 andesite sample (cubic voxels of width 23 μm).

Figure 3. Porosity structure. (a) 3D image of an undeformed andesite sample (LL3), created using the X-ray image slices (23 μm /voxel), showing the porosity structure. Each connected pore is shown in a different colour. (b) The same 3D image shown in panel (a), but with the large, connected pore (coloured dark blue in panel (a)) removed. (c) Histogram showing the distribution of pore radii for the unconnected pores shown in panel (b).

Figure 4. Mechanical data. (a) Stress-strain curve for the sample (LL5) deformed at an effective pressure of 10 MPa (in the brittle regime). (b) Stress-strain curve for the sample (LL3) deformed at an effective pressure of 50 MPa (in the ductile regime). (c) Porosity reduction as a function of axial strain for the sample (LL5) deformed at an effective pressure of 10 MPa (in the brittle regime). (d) Porosity reduction as a function of axial strain for the

sample (LL3) deformed at an effective pressure of 50 MPa (in the ductile regime). The positions of the X-ray scans are indicated on the stress-strain curves.

Figure 5. Porosity profiles. (a) Porosity as a function of sample length (sample LL5) before and after deformation at an effective pressure of 10 MPa (in the brittle regime). (b) Porosity as a function of sample length (sample LL3) before and after one and two rounds of deformation (see Figure 4b) at an effective pressure of 50 MPa (in the ductile regime).

Figure 6. Digital volume correlation data. (a) Divergence (volumetric strain) and curl (a proxy for shear strain) of the displacement field for the sample (LL5) deformed at an effective pressure of 10 MPa (in the brittle regime). (b) Divergence (volumetric strain) and curl (shear strain) for the sample (LL3) following the first round of deformation (see Figure 4c) at an effective pressure of 50 MPa (in the ductile regime). (c) Divergence (volumetric strain) and curl (shear strain) for the sample (LL3) following the second round of deformation (see Figure 4c) at an effective pressure of 50 MPa (in the ductile regime).

Figure 7. 2D vertical slices extracted from the 3D tomography data volume of the intact LL3 sample and the same sample following the first round of deformation at an effective pressure of 50 MPa (in the ductile regime). This image shows the compaction band at the top of the sample that was missed by the porosity and DVC analyses. The lower image shows a zoomed image in which collapsed pores are highlighted by white arrows.

References

- Adelinet, M., Fortin, J., Schubnel, A., & Guéguen, Y. (2013). Deformation modes in an Icelandic basalt: from brittle failure to localized deformation bands. *Journal of Volcanology and Geothermal Research*, 255, 15-25.
- Anderson, S. W., & Fink, J. H. (1990). The development and distribution of surface textures at the Mount St. Helens dome. In *Lava flows and domes* (pp. 25-46). Springer, Berlin, Heidelberg.
- Baker, D. R., Polacci, M., & LaRue, A. (2011). A study on the reproducibility of counting vesicles in volcanic rocks. *Geosphere*, 7(1), 70-78.
- Baud, P., Klein, E., & Wong, T.-f. (2004). Compaction localization in porous sandstones: spatial evolution of damage and acoustic emission activity. *Journal of Structural Geology*, 26(4), 603-624.
- Baud, P., Meredith, P., & Townend, E. (2012). Permeability evolution during triaxial compaction of an anisotropic porous sandstone. *Journal of Geophysical Research: Solid Earth*, 117(B5).
- Baud, P., Reuschlé, T., Ji, Y., Cheung, C. S., & Wong, T.-f. (2015). Mechanical compaction and strain localization in Bleurswiller sandstone. *Journal of Geophysical Research: Solid Earth*, 120(9), 6501-6522.
- Bauer, D., Youssef, S., Fleury, M., Bekri, S., Rosenberg, E., & Vizika, O. (2012). Improving the estimations of petrophysical transport behavior of carbonate rocks using a dual pore network approach combined with computed microtomography. *Transport in porous media*, 94(2), 505-524.
- Benson, P. M., Thompson, B. D., Meredith, P. G., Vinciguerra, S., & Young, R. P. (2007). Imaging slow failure in triaxially deformed Etna basalt using 3D acoustic-emission location and X-ray computed tomography. *Geophysical Research Letters*, 34(3).
- Benson, P. M., Heap, M. J., Lavallée, Y., Flaws, A., Hess, K. U., Selvadurai, A. P. S., ... & Schillinger, B. (2012). Laboratory simulations of tensile fracture development in a volcanic conduit via cyclic magma pressurisation. *Earth and Planetary Science Letters*, 349, 231-239.
- Bésuelle, P. (2001). Evolution of strain localisation with stress in a sandstone: brittle and semi-brittle regimes. *Physics and Chemistry of the Earth, Part A: Solid Earth and Geodesy*, 26(1-2), 101-106.
- Bésuelle, P., Baud, P., & Wong, T.-f. (2003). Failure mode and spatial distribution of damage in Rothbach sandstone in the brittle-ductile transition. In *Thermo-Hydro-Mechanical Coupling in Fractured Rock* (pp. 851-868). Birkhäuser, Basel.

- Black, B. A., Manga, M., & Andrews, B. (2016). Ash production and dispersal from sustained low-intensity Mono-Inyo eruptions. *Bulletin of Volcanology*, 78(8), 57.
- Brace, W. F., Paulding Jr, B. W., & Scholz, C. H. (1966). Dilatancy in the fracture of crystalline rocks. *Journal of Geophysical Research*, 71(16), 3939-3953.
- Bubeck, A., Walker, R. J., Healy, D., Dobbs, M., & Holwell, D. A. (2017). Pore geometry as a control on rock strength. *Earth and Planetary Science Letters*, 457, 38-48.
- Bubeck, A., Walker, R. J., Imber, J., & MacLeod, C. J. (2018). Normal fault growth in layered basaltic rocks: The role of strain rate in fault evolution. *Journal of Structural Geology*, 115, 103-120.
- Bull, K. F., Anderson, S. W., Diefenbach, A. K., Wessels, R. L., & Henton, S. M. (2013). Emplacement of the final lava dome of the 2009 eruption of Redoubt Volcano, Alaska. *Journal of Volcanology and Geothermal Research*, 259, 334-348.
- Caine, J. S., Evans, J. P., & Forster, C. B. (1996). Fault zone architecture and permeability structure. *Geology*, 24(11), 1025-1028.
- Cashman, K. V., Thornber, C. R., & Pallister, J. S. (2006). *From dome to dust: Shallow crystallization and fragmentation of conduit magma during the 2004-2006 dome extrusion of Mount St. Helens, Washington* (No. 1750-19, pp. 387-413). US Geological Survey.
- Cassidy, M., Manga, M., Cashman, K., & Bachmann, O. (2018). Controls on explosive-effusive volcanic eruption styles. *Nature Communications*, 9(1), 1-16.
- Castro, J. M., Dingwell, D. B., Nichols, A. R., & Gardner, J. E. (2005). New insights on the origin of flow bands in obsidian. *Special Papers - Geological Society of America*, 396, 55.
- Castro, J. M., Bindeman, A. R., Tuffen, H., & Schipper, C. I. (2014). Explosive origin of silicic lava: textural and $\delta D-H_2O$ evidence for pyroclastic degassing during rhyolite effusion. *Earth and Planetary Science Letters*, 405, 52-61.
- Cavailles, T., & Rotevatn, A. (2018). Deformation bands in volcanoclastic rocks—Insights from the Shihtiping tuffs, Coastal Range of Taiwan. *Journal of Structural Geology*, 113, 155-175.
- Charalampidou, E. M., Hall, S. A., Stanchits, S., Viggiani, G., & Lewis, H. (2010). Characterization of Shear and Compaction Bands in Sandstone Using X-Ray Tomography and 3D Digital Image Correlation. *Advances in Computed Tomography for Geomaterials: GeoX 2010*, 59-66.

- Charalampidou, E. M., Hall, S. A., Stanchits, S., Lewis, H., & Viggiani, G. (2011). Characterization of shear and compaction bands in a porous sandstone deformed under triaxial compression. *Tectonophysics*, *503*(1-2), 8-17.
- Cilona, A., Faulkner, D. R., Tondi, E., Agosta, F., Mancini, L., Rustichelli, A., ... & Vinciguerra, S. (2014). The effects of rock heterogeneity on compaction localization in porous carbonates. *Journal of Structural Geology*, *67*, 75-93.
- Coats, R., Kendrick, J. E., Wallace, P. A., Miwa, T., Hornby, A. J., Ashworth, J. D., ... & Lavallée, Y. (2018). Failure criteria for porous dome rocks and lavas: a study of Mt. Unzen, Japan. *Solid Earth*, *9*(6), 1299-1328.
- Cole, P. D., Calder, E. S., Druitt, T. H., Hoblitt, R., Robertson, R., Sparks, L. S. J., & Young, S. R. (1998). Pyroclastic flows generated by gravitational instability of the 1916–97 lava dome of Soufriere Hills Volcano, Montserrat. *Geophysical Research Letters*, *25*(15), 3425-3428.
- Collinson, A. S. D., & Neuberg, J. W. (2012). Gas storage, transport and pressure changes in an evolving permeable volcanic edifice. *Journal of Volcanology and Geothermal Research*, *243*, 1-13.
- Darmawan, H., Walter, T. R., Brotopuspito, K. S., & Nandaka, I. G. M. A. (2018). Morphological and structural changes at the Merapi lava dome monitored in 2012–15 using unmanned aerial vehicles (UAVs). *Journal of Volcanology and Geothermal Research*, *349*, 256-267.
- Dautriat, J., Bornert, M., Gland, N., Dimantov, A., & Raphanel, J. (2011). Localized deformation induced by heterogeneities in porous carbonate analysed by multi-scale digital image correlation. *Tectonophysics*, *503*(1-2), 100-116.
- Degruyter, W., Burgisser, A., Bachmann, O., & Malaspina, O. (2010). Synchrotron X-ray microtomography and lattice Boltzmann simulations of gas flow through volcanic pumices. *Geosphere*, *6*(5), 470-481.
- Eggertsson, G. H., Lavallée, Y., Kendrick, J. E., & Markússon, S. H. (2018). Improving fluid flow in geothermal reservoirs by thermal and mechanical stimulation: The case of Krafla volcano, Iceland. *Journal of Volcanology and Geothermal Research*.
- Eichelberger, J. C., Carrigan, C. R., Westrich, H. R., & Price, R. H. (1986). Non-explosive silicic volcanism. *Nature*, *323*(6089), 598-602.
- Farquharson, J. I., Heap, M. J., Lavallée, Y., Varley, N. R., & Baud, P. (2016a). Evidence for the development of permeability anisotropy in lava domes and volcanic conduits. *Journal of Volcanology and Geothermal Research*, *323*, 163-185.

- Farquharson, J. I., Heap, M. J., & Baud, P. (2016b). Strain-induced permeability increase in volcanic rock. *Geophysical Research Letters*, *43*(22), 11-603.
- Farquharson, J. I., Baud, P., & Heap, M. J. (2017). Inelastic compaction and permeability evolution in volcanic rock. *Solid Earth*, *8*(2), 561.
- Farquharson, J. I., & Wadsworth, F. B. (2018). Upscaling permeability in anisotropic volcanic systems. *Journal of Volcanology and Geothermal Research*, *364*, 35-47.
- Fortin, J., Stanchits, S., Dresen, G., & Guéguen, Y. (2006). Acoustic emission and velocities associated with the formation of compaction bands in sandstone. *Journal of Geophysical Research: Solid Earth*, *111*(B10).
- Fortin, J., Stanchits, S., Vinciguerra, S., & Guéguen, Y. (2011). Influence of thermal and mechanical cracks on permeability and elastic wave velocities in a basalt from Mt. Etna volcano subjected to elevated pressure. *Tectonophysics*, *503*(1-2), 60-74.
- Fusseis, F., Schrank, C., Liu, J., Karrech, A., Llana-Funez, S., Xiao, X., & Regenauer-Lieb, K. (2012). Pore formation during dehydration of polycrystalline gypsum observed and quantified in a time-series synchrotron radiation based X-ray micro-tomography experiment. *Solid Earth*, *3*(1), 71-86.
- Gardner, J. E., Wadsworth, F. B., Llewellyn, E. W., Watkins, J. M., & Coumans, J. P. (2018). Experimental sintering of ash at conduit conditions and implications for the longevity of tuffsites. *Bulletin of Volcanology*, *80*(3), 23.
- Giachetti, T., Burgisser, A., Arbaret, L., Druitt, T. H., & Kelfoun, K. (2011). Quantitative textural analysis of Vulcanian pyroclasts (Montserrat) using multi-scale X-ray computed microtomography: comparison with results from 2D image analysis. *Bulletin of Volcanology*, *73*(9), 1295-1309.
- Glicken, H. (1996). *Rockslide debris avalanche of May 18, 1980, Mount St. Helens volcano, Washington* (No. 96-677). US Geological Survey.
- Gonnermann, H. M., & Manga, M. (2005). Flow banding in obsidian: A record of evolving textural heterogeneity during magma deformation. *Earth and Planetary Science Letters*, *236*(1-2), 135-147.
- Gudmundsson, A. (2011). *Rock fractures in geological processes*. Cambridge University Press.
- Hale, A. J., & Wadge, G. (2008). The transition from endogenous to exogenous growth of lava domes with the development of shear bands. *Journal of Volcanology and Geothermal Research*, *171*(3-4), 237-257.

- Heap, M. J., Lavallée, Y., Petrakova, L., Baud, P., Reuschlé, T., Varley, N. R., & Dingwell, D. B. (2014). Microstructural controls on the physical and mechanical properties of edifice-forming andesites at Volcán de Colima, Mexico. *Journal of Geophysical Research: Solid Earth*, *119*(4), 2925-2963.
- Heap, M. J., Farquharson, J. I., Baud, P., Lavallée, Y., & Reuschlé, T. (2015a). Fracture and compaction of andesite in a volcanic edifice. *Bulletin of Volcanology*, *77*(6), 55.
- Heap, M. J., Brantut, N., Baud, P., & Meredith, P. G. (2015b). Time-dependent compaction band formation in sandstone. *Journal of Geophysical Research: Solid Earth*, *120*(7), 4808-4830.
- Heap, M. J., & Wadsworth, F. B. (2016). Closing an open system: pore pressure changes in permeable edifice rock at high strain rates. *Journal of Volcanology and Geothermal Research*, *315*, 40-50.
- Heap, M. J., & Kennedy, B. M. (2016). Exploring the scale-dependent permeability of fractured andesite. *Earth and Planetary Science Letters*, *447*, 139-150.
- Heap, M. J., Russell, J. K., & Kennedy, L. A. (2016). Mechanical behaviour of dacite from Mount St. Helens (USA): A link between porosity and lava dome extrusion mechanism (dome or spine)? *Journal of Volcanology and Geothermal Research*, *328*, 159-171.
- Heap, M. J., Violay, M., Wadsworth, F. B., & Massour, J. (2017). From rock to magma and back again: the evolution of temperature and deformation mechanism in conduit margin zones. *Earth and Planetary Science Letters*, *463*, 92-100.
- Heap, M. J., Coats, R., Chen, C. F., Varley, N., Lavallée, Y., Kendrick, J., ... & Reuschlé, T. (2018). Thermal resilience of microcracked andesitic dome rocks. *Journal of Volcanology and Geothermal Research*, *367*, 20-30.
- Heap, M. J., Tuffen, H., Wadsworth, F. B., Reuschlé, T., Castro, J. M., & Schipper, C. I. (2019a). The permeability evolution of tuffisites and implications for outgassing through dense rhyolitic magma. *Journal of Geophysical Research: Solid Earth*, *124*(8), 8281-8299.
- Heap, M. J., Troll, V. R., Kushnir, A. R., Gilg, H. A., Collinson, A. S., Deegan, F. M., ... & Walter, T. R. (2019b). Hydrothermal alteration of andesitic lava domes can lead to explosive volcanic behaviour. *Nature Communications*, *10*(1), 1-10.
- Hill, R.E. (1989). Analysis of Deformation Bands in the Aztec Sandstone. Valley of Fire State Park, Nevada. Master Thesis, Univ. Nevada, Las Vegas.
- Holland, M., Urai, J. L., & Martel, S. (2006). The internal structure of fault zones in basaltic sequences. *Earth and Planetary Science Letters*, *248*(1-2), 301-315.

- Hornby, A. J., Kendrick, J. E., Lamb, O. D., Hirose, T., De Angelis, S., von Aulock, F. W., ... & Hess, K. U. (2015). Spine growth and seismogenic faulting at Mt. Unzen, Japan. *Journal of Geophysical Research: Solid Earth*, *120*(6), 4034-4054.
- Huang, L., Baud, P., Cordonnier, B., Renard, F., Liu, L., & Wong, T.-f. (2019). Synchrotron X-ray imaging in 4D: Multiscale failure and compaction localization in triaxially compressed porous limestone. *Earth and Planetary Science Letters*, *528*, 115831.
- Iverson, R. M., Dzurisin, D., Gardner, C. A., Gerlach, T. M., LaHusen, R. G., Lisowski, M., ... & Pallister, J. S. (2006). Dynamics of seismogenic volcanic extrusion at Mount St Helens in 2004–05. *Nature*, *444*(7118), 439-443.
- Jamtveit, B., Kobchenko, M., Austrheim, H., Malthe-Sørenssen, A., Røyne, A., & Svensen, H. (2011). Porosity evolution and crystallization-driven fragmentation during weathering of andesite. *Journal of Geophysical Research: Solid Earth*, *116*(B12).
- Jamtveit, B., Krotkiewski, M., Kobchenko, M., Renard, F., & Angier-Luta, L. (2014). Pore-space distribution and transport properties of an andesitic intrusion. *Earth and Planetary Science Letters*, *400*, 123-129.
- Ji, Y., Baud, P., Vajdova, V., & Wong, T.-f. (2012). Characterization of pore geometry of Indiana limestone in relation to mechanical compaction. *Oil & Gas Science and Technology—Revue d'IFP Energies Nouvelles*, *67*(5), 753-775.
- Ji, Y., Hall, S. A., Baud, P., & Wong, T.-f. (2015). Characterization of pore structure and strain localization in Majella limestone by X-ray computed tomography and digital image correlation. *Geophysical Journal International*, *200*(2), 701-719.
- Kandula, N., Cordonnier, B., Poller, E., Weiss, J., Dysthe, D. K., & Renard, F. (2019). Dynamics of microscale precursors during brittle compressive failure in Carrara marble. *Journal of Geophysical Research: Solid Earth*, *124*(6), 6121-6139.
- Kendrick, J. E., Lavallée, Y., Hess, K. U., Heap, M. J., Gaunt, H. E., Meredith, P. G., & Dingwell, D. B. (2013). Tracking the permeable porous network during strain-dependent magmatic flow. *Journal of Volcanology and Geothermal Research*, *260*, 117-126.
- Kennedy, L. A., & Russell, J. K. (2012). Cataclastic production of volcanic ash at Mount Saint Helens. *Physics and Chemistry of the Earth, Parts A/B/C*, *45*, 40-49.
- Komorowski, J. C., Jenkins, S., Baxter, P. J., Picquout, A., Lavigne, F., Charbonnier, S., ... & Budi-Santoso, A. (2013). Paroxysmal dome explosion during the Merapi 2010 eruption: Processes and facies relationships

- of associated high-energy pyroclastic density currents. *Journal of Volcanology and Geothermal Research*, 261, 260-294.
- Lagmay, A. M. F., De Vries, B. V. W., Kerle, N., & Pyle, D. M. (2000). Volcano instability induced by strike-slip faulting. *Bulletin of Volcanology*, 62(4-5), 331-346.
- Lamb, O. D., De Angelis, S., Umakoshi, K., Hornby, A. J., Kendrick, J. E., & Lavallée, Y. (2015). Repetitive fracturing during spine extrusion at Unzen volcano, Japan. *Solid Earth*, 6(4), 1277-1293.
- Lavallée, Y., Benson, P. M., Heap, M. J., Hess, K. U., Flaws, A., Schillinger, B., ... & Dingwell, D. B. (2013). Reconstructing magma failure and the degassing network of dome-building eruptions. *Geology*, 41(4), 515-518.
- Lindquist, W. B., Venkatarangan, A., Dunsmuir, J., & Wong, T.-f. (2010). Pore and throat size distributions measured from synchrotron X-ray tomographic images of Fontainebleau sandstones. *Journal of Geophysical Research: Solid Earth*, 105(B9), 21509-21527.
- Loaiza, S., Fortin, J., Schubnel, A., Guéguen, Y., Vinciguerra, S., & Moreira, M. (2012). Mechanical behavior and localized failure modes in a porous basalt from the Azores. *Geophysical Research Letters*, 39(19).
- Lockner, D. (1993). The role of acoustic emission in the study of rock fracture. *International Journal of Rock Mechanics and Mining Sciences & Geomechanics Abstracts*, 30, No. 7, 883-899.
- Louis, L., Wong, T.-f., Baud, P., & Terres, J. (2006). Imaging strain localization by X-ray computed tomography: discrete compaction bands in Diemelstadt sandstone. *Journal of Structural Geology*, 28(5), 762-775.
- Louis, L., Wong, T.-f., & Baud, P. (2007). Imaging strain localization by X-ray radiography and digital image correlation: Deformation bands in Rothbach sandstone. *Journal of Structural Geology*, 29(1), 129-140.
- McBeck, J., Kobchenko, M., Hall, S. A., Tudisco, E., Cordonnier, B., Meakin, P., & Renard, F. (2018). Investigating the onset of strain localization within anisotropic shale using digital volume correlation of time-resolved X-ray microtomography images. *Journal of Geophysical Research: Solid Earth*, 123(9), 7509-7528.
- McBeck, J. A., Cordonnier, B., Vinciguerra, S., & Renard, F. (2019). Volumetric and shear strain localization in Mt. Etna basalt. *Geophysical Research Letters*, 46(5), 2425-2433.
- McBeck, J., Ben-Zion, Y., & Renard, F. (2020). The mixology of precursory strain partitioning approaching brittle failure in rocks. *Geophysical Journal International*, 221(3), 1856-1872.

- Mitchell, T. M., & Faulkner, D. R. (2008). Experimental measurements of permeability evolution during triaxial compression of initially intact crystalline rocks and implications for fluid flow in fault zones. *Journal of Geophysical Research: Solid Earth*, 113(B11).
- Mollema, P. N., & Antonellini, M. A. (1996). Compaction bands: a structural analog for anti-mode I cracks in aeolian sandstone. *Tectonophysics*, 267(1-4), 209-228.
- Mueller, S., Scheu, B., Spieler, O., & Dingwell, D. B. (2008). Permeability control on magma fragmentation. *Geology*, 36(5), 399-402.
- Moran, P. A. (1948). The interpretation of statistical maps. *Journal of the Royal Statistical Society. Series B (Methodological)*, 10(2), 243-251.
- Nara, Y., Meredith, P. G., Yoneda, T., & Kaneko, K. (2011). Influence of macro-fractures and micro-fractures on permeability and elastic wave velocities in basalt at elevated pressure. *Tectonophysics*, 503(1-2), 52-59.
- Okubo, C. H. (2014). Brittle deformation and slope failure at the North Menan butte tuff cone, eastern Snake River plain, Idaho. *Journal of Volcanology and Geothermal Research*, 278, 86-95.
- Pardo, N., Cronin, S. J., Wright, H. M., Schipper, C. L., Smith, I., & Stewart, B. (2014). Pyroclast textural variation as an indicator of eruption column steadiness in andesitic Plinian eruptions at Mt. Ruapehu. *Bulletin of Volcanology*, 76(5), 822.
- Polacci, M., Baker, D. R., Mancini, L., Tronola, G., & Zanini, F. (2006). Three-dimensional investigation of volcanic textures by X-ray microtomography and implications for conduit processes. *Geophysical Research Letters*, 33(13).
- Renard, F., Cordonnier, B., Kochenko, M., Kandula, N., Weiss, J., & Zhu, W. (2017). Microscale characterization of pore nucleation unravels precursors to faulting in rocks. *Earth and Planetary Science Letters*, 476, 69-78.
- Renard, F., McBeck, J., Cordonnier, B., Zheng, X., Kandula, N., Sanchez, J. R., ... & Fousseis, F. (2019). Dynamic in situ three-dimensional imaging and digital volume correlation analysis to quantify strain localization and fracture coalescence in sandstone. *Pure and Applied Geophysics*, 176(3), 1083-1115.
- Rotevatn, A., Thorsheim, E., Bastesen, E., Fossmark, H. S., Torabi, A., & Sælen, G. (2016). Sequential growth of deformation bands in carbonate grainstones in the hangingwall of an active growth fault: Implications for deformation mechanisms in different tectonic regimes. *Journal of Structural Geology*, 90, 27-47.

- Rust, A. C., Manga, M., & Cashman, K. V. (2003). Determining flow type, shear rate and shear stress in magmas from bubble shapes and orientations. *Journal of Volcanology and Geothermal Research*, 122(1-2), 111-132.
- Rust, A. C., Cashman, K. V., & Wallace, P. J. (2004). Magma degassing buffered by vapor flow through brecciated conduit margins. *Geology*, 32(4), 349-352.
- Rutter, E. H. (1986). On the nomenclature of mode of failure transitions in rocks. *Tectonophysics*, 122(3-4), 381-387.
- Ryan, A. G., Friedlander, E. A., Russell, J. K., Heap, M. J., & Kennedy, L. A. (2018). Hot pressing in conduit faults during lava dome extrusion: Insights from Mount St. Helens, 2004–2008. *Earth and Planetary Science Letters*, 482, 171-180.
- Ryan, A. G., Heap, M. J., Russell, J. K., Kennedy, L. A., & M. Clyne (2020). Cyclic shear zone cataclasis and sintering during lava dome extrusion: Insights from Chaos Crags, Lassen Volcanic Center (USA). *Journal of Volcanology and Geothermal Research*. Accepted.
- Saubin, E., Tuffen, H., Gurioli, L., Owen, J., Castro, J. M., Berro, K., ... & Wehbe, K. (2016). Conduit dynamics in transitional rhyolitic activity recorded by tuffisite vein textures from the 2008–2009 Chaitén Eruption. *Frontiers in Earth Science*, 4, 59.
- Schipper, C. I., Mandon, C., Maksimenko, A., Castro, J. M., Conway, C. E., Hauer, P., ... & Kilgour, G. (2017). Vapor-phase cristobalite as a durable indicator of magmatic pore structure and halogen degassing: an example from White Island volcano (New Zealand). *Bulletin of Volcanology*, 79(10), 74.
- Scholz, C. H. (1968). Microfracturing and the inelastic deformation of rock in compression. *Journal of Geophysical Research*, 73(4), 1417-1432.
- Shea, T., Houghton, B. F., Gurioli, L., Cashman, K. V., Hammer, J. E., & Hobden, B. J. (2010). Textural studies of vesicles in volcanic rocks: an integrated methodology. *Journal of Volcanology and Geothermal Research*, 190(3-4), 271-289.
- Shahin, G., Papazoglou, A., Marinelli, F., & Buscarnera, G. (2019). Simulation of localized compaction in Tuffeau de Maastricht based on evidence from X-ray tomography. *International Journal of Rock Mechanics and Mining Sciences*, 121, 104039.
- Song, S. R., Jones, K. W., Lindquist, B. W., Dowd, B. A., & Sahagian, D. L. (2001). Synchrotron X-ray computed microtomography: studies on vesiculated basaltic rocks. *Bulletin of Volcanology*, 63(4), 252-263.

- Thompson, E. S., Saveyn, P., Declercq, M., Meert, J., Guida, V., Eads, C. D., Robles, E. S. J., & Britton, M. M. (2018). Characterisation of heterogeneity and spatial autocorrelation in phase separating mixtures using Moran's I. *Journal of Colloid and Interface Science*, 513, 180-187.
- Townend, E., Thompson, B. D., Benson, P. M., Meredith, P. G., Baud, P., & Young, R. P. (2008). Imaging compaction band propagation in Diemelstadt sandstone using acoustic emission locations. *Geophysical Research Letters*, 35(15).
- Tudisco, E., Hall, S. A., Charalampidou, E. M., Kardjilov, N., Hilger, A., & Sone, H. (2015). Full-field measurements of strain localisation in sandstone by neutron tomography and 3D-volumetric digital image correlation. *Physics Procedia*, 69(509-515).
- Tudisco, E., Andò, E., Cailletaud, R., & Hall, S. A. (2017). TomoWave2: a local digital volume correlation code. *SoftwareX*, 6, 267-270.
- Tuffen, H., Dingwell, D. B., & Pinkerton, H. (2003). Repeated fracture and healing of silicic magma generate flow banding and earthquakes? *Geology*, 31(12), 1089-1092.
- Varley, N., Connor, C. B., & Komorowski, J. C. (Eds.). (2019). *Volcán de Colima: Portrait of a Persistently Hazardous Volcano*. Springer.
- Voight, B. (2000). Structural stability of andesite volcanoes and lava domes. *Philosophical Transactions of the Royal Society of London. Series A: Mathematical, Physical and Engineering Sciences*, 358(1770), 1663-1703.
- Voltolini, M., Zandomenighi, D., Mancini, L., & Polacci, M. (2011). Texture analysis of volcanic rock samples: quantitative study of crystals and vesicles shape preferred orientation from X-ray microtomography data. *Journal of Volcanology and Geothermal Research*, 202(1-2), 83-95.
- Wadsworth, F. B., Vasseur, J., Llewellyn, E. W., Dobson, K. J., Colombier, M., Von Aulock, F. W., ... & Lavallée, Y. (2017). Topological inversions in coalescing granular media control fluid-flow regimes. *Physical Review E*, 96(3), 033113.
- Wadsworth, F. B., Vasseur, J., Schaubert, J., Llewellyn, E. W., Dobson, K. J., Havard, T., ... & Hess, K. U. (2019). A general model for welding of ash particles in volcanic systems validated using in situ X-ray tomography. *Earth and Planetary Science Letters*, 525, 115726.
- Walker, R. J., Holdsworth, R. E., Armitage, P. J., & Faulkner, D. R. (2013). Fault zone permeability structure evolution in basalts. *Geology*, 41(1), 59-62.

- Walker, R. J., Holdsworth, R. E., Imber, J., Faulkner, D. R., & Armitage, P. J. (2013). Fault zone architecture and fluid flow in interlayered basaltic volcanoclastic-crystalline sequences. *Journal of Structural Geology*, *51*, 92-104.
- Walter, T. R., Subandriyo, J., Kirbani, S., Bathke, H., Suryanto, W., Aisyah, N., ... & Dahm, T. (2015). Volcano-tectonic control of Merapi's lava dome splitting: The November 2013 fracture observed from high resolution TerraSAR-X data. *Tectonophysics*, *639*, 23-33.
- Wang, B., Chen, Y., & Wong, T.-f. (2008). A discrete element model for the development of compaction localization in granular rock. *Journal of Geophysical Research: Solid Earth*, *113*(B3).
- Watts, R. B., Herd, R. A., Sparks, R. S. J., & Young, S. R. (2002). Growth patterns and emplacement of the andesitic lava dome at Soufriere Hills Volcano, Montserrat. *Geological Society, London, Memoirs*, *21*(1), 115-152.
- Wilson, J. E., Goodwin, L. B., & Lewis, C. J. (2003). Deformation bands in nonwelded ignimbrites: Petrophysical controls on fault-zone deformation and evidence of preferential fluid flow. *Geology*, *31*(10), 837-840.
- Zandomenighi, D., Voltolini, M., Mancini, L., Brun, F., Dreossi, D., & Polacci, M. (2010). Quantitative analysis of X-ray microtomography images of geomaterials: Application to volcanic rocks. *Geosphere*, *6*(6), 793-804.
- Zhang, T., & Lin, G. (2016). On Moran's I coefficient under heterogeneity. *Computational Statistics & Data Analysis*, *95*, 83-94.
- Zhu, W., Baud, P., Vinciguerra, S., & Wong, T.-f. (2011). Micromechanics of brittle faulting and cataclastic flow in Alban Hills tuff. *Journal of Geophysical Research: Solid Earth*, *116*(B6).
- Zhu, W., Baud, P., Vinciguerra, S., & Wong, T. F. (2016). Micromechanics of brittle faulting and cataclastic flow in Mount Etna basalt. *Journal of Geophysical Research: Solid Earth*, *121*(6), 4268-4289.
- Zhu, W., & Wong, T.-f. (1997). The transition from brittle faulting to cataclastic flow: Permeability evolution. *Journal of Geophysical Research: Solid Earth*, *102*(B2), 3027-3041.

Imaging strain localisation in porous andesite using digital volume correlation

Michael J. Heap, Patrick Baud, Jessica A. McBeck, François Renard, Lucille Carbillet, and Stephan A. Hall

Author statement

Michael J. Heap: Conceptualisation, Investigation, Writing - Original Draft, Visualisation, Project Administration. **Patrick Baud:** Conceptualisation, Investigation, Writing – Review & Editing, Project Administration. **Jessica A. McBeck:** Formal analysis, Writing – Review & Editing, Visualisation. **François Renard:** Formal analysis, Writing – Review & Editing, Visualisation. **Lucille Carbillet:** Formal analysis, Writing – Review & Editing. **Stephan A. Hall:** Formal analysis, Investigation, Writing – Review & Editing.

Declaration of interests

The authors declare that they have no known competing financial interests or personal relationships that could have appeared to influence the work reported in this paper.

The authors declare the following financial interests/personal relationships which may be considered as potential competing interests:

Journal Pre-proof

Imaging strain localisation in porous andesite using digital volume correlation

Michael J. Heap, Patrick Baud, Jessica A. McBeck, François Renard, Lucille Carbillet, and Stephan A. Hall

Highlights

- Shear fractures associated with localised dilation and permeability increase.
- Compaction bands associated with localised compaction and permeability decrease.
- Compaction bands form in the most porous part of the sample, within the well-connected porosity backbone.
- Geometric characteristics of compaction bands in lavas likely related to pore size and structure.
- Digital volume correlation is a useful tool to study strain localisation in porous volcanic rocks.